Materials Advances

ROYAL SOCIETY OF CHEMISTRY

PAPER

View Article Online
View Journal | View Issue

Cite this: *Mater. Adv.*, 2026, 7, 2047

Revisiting bimodal cancer phototherapy with immunogenicity *via* galvanically-driven hollow Pd–As nanoshells

Sun Woo Kim,†[a] Manorma Negi,†[b] Youbin Heo,[a] Apurva Jaiswal,[b] Eun Ha Choi,[b] Neha Kaushik,*[c] Hongje Jang *[a] and Nagendra Kumar Kaushik *[b]

Most cases of lung cancer are non-small cell lung cancer (NSCLC), and because there are still tumor tissues near the treatment margins, it is challenging to completely eradicate the cancer and prevent metastasis and recurrence. The application of tumor phototherapy, including photodynamic therapy (PDT) and photothermal therapy (PTT), has been considered an effective strategy for achieving significant immunogenic cell death (ICD) at optimal tumor retention. Arsenic (As) is recognized as toxic to both the environment and human health. However, historically, arsenic was employed in medicine for the treatment of syphilis and psoriasis and served as a standard remedy for blood diseases such as anaemia and subsequently leukaemia. It can have its toxicity mitigated through engineering with other non-toxic metals, such as palladium (Pd), thereby facilitating safer, localized therapeutic applications. In this study, novel arsenic nanoparticles (NPs) with rough surface morphology were transformed into hollow Pd–As nanoshells (PdAsNPs) *via* an optimized galvanic replacement reaction. The NPs generated heat and singlet oxygen upon irradiation with an 808-nm near-infrared laser owing to the presence of Pd. PdAsNPs not only showed biocompatibility with normal lung cells but also induced hyperthermia and generated reactive oxygen species in A549 human lung cancer cells, thus demonstrating their potential for combined photothermal and photodynamic therapy. Laser-irradiated PdAsNPs also increased the expression of antioxidant genes in cancer cells. This combination therapy amplifies immunogenic cell death by releasing damage-associated molecular patterns, such as HMGB1 and CRT, while preventing the immune escape protein CD47. Our bimodal photo-triggered combination therapy demonstrated synergistic anticancer activity at safe doses for potential practical applications.

Received 21st July 2025,
Accepted 9th October 2025

DOI: 10.1039/d5ma00784d

rsc.li/materials-advances

1. Introduction

Arsenic (As), commonly found in contaminated groundwater, industrial wastewater, tobacco, and pesticides, has long been recognized as a toxic substance.[1–3] However, it is also used in the construction of semiconductor materials,[4,5] such as light-emitting diodes,[6,7] and As oxides have been used in anticancer applications.[8–10] Notably, metallic As nanoparticles (As NPs) are less toxic than inorganic or organic As, and researchers have attempted to synthesize As oxide NPs.[11,12] Moreover, researchers have shown interest in exploiting the oxidation resistance of As, which is lower than that of noble metals, for spontaneous elemental substitution and structural modification.[13] Complex structures such as hollow nanoshells, nanocages, and nanoframes synthesized *via* post-synthesis structural control typically exhibit photothermal conversion or photocatalytic radical generation upon absorption of long-wavelength light.[14–16] Notably, NPs of a certain size (20–300 nm) exhibit a synergistic effect with photodynamic therapy (PDT) and photothermal therapy (PTT) as they accumulate in the tumor tissue.[17–21]

Unlike PDT, PTT does not depend on oxygen to interact with target cells or tissues. In PTT, the photosensitizer vibrates to generate heat, which selectively eliminates tumor cells over normal tissues because tumor cells are more sensitive to the microenvironment at high temperatures.[18,19] Moreover, PTT does not have side effects and exhibits desirable specificity and repeatability. The blood vessels in and around the tumor have different characteristics from normal blood vessels, including poor lymphatic drainage and disorganized leakage, because tumors have higher concentrations of certain particles

[a] *Department of Chemistry, Kwangwoon University, 20 Gwangwoon-ro, Nowon-gu, Seoul 01897, Republic of Korea. E-mail: hjang@kw.ac.kr*
[b] *Plasma Bioscience Research Center, Department of Electrical and Biological Physics, Kwangwoon University, Seoul, 01897, Republic of Korea. E-mail: kaushik.nagendra@kw.ac.kr*
[c] *Department of Biotechnology, College of Engineering, The University of Suwon, Hwaseong, 18323, Republic of Korea. E-mail: neha.bioplasma@gmail.com*
† Mr S. W. Kim and M. Negi contributed equally to this study.

than other body parts. In this context, multifunctional NPs have been developed for PDT and PTT.[20,21] Hyperthermia caused by PTT enhances vascular permeability and the formation of reactive oxygen species (ROS), which have a synergistic anti-cancer effect with other modalities, such as chemotherapy, radiotherapy, and thermodynamic therapy. PTT-induced hyperthermia in tumor tissues accelerates the Fenton reaction to produce a greater number of hydroxyl radicals ($OH^{\bullet}$), thus increasing oxidative stress in the tumor tissue and resulting in cell death.[22,23] A combination of PTT, PDT, and NPs causes immunogenic cell death (ICD) in cancer cells and promotes long-term survival of cancer patients.[21,24–26] Previous studies have shown that NPs of a certain size (20–300 nm) exhibit a synergistic effect with PDT and PTT as they accumulate in tumor tissue. However, designing innovative nanomaterials that can maximize the efficacy of these therapies and induce a robust antitumor immune response remains a significant research challenge.

Herein, we report a new synthetic approach to convert arsenic nanoparticles (AsNPs) with a unique rough surface morphology into hollow Pd–As nanoshells (PdAsNPs) *via* an optimized galvanic replacement reaction. This unique nanostructure leverages the plasmonic properties of Pd to generate heat and singlet oxygen upon irradiation with an 808-nm near-infrared (NIR) laser, demonstrating its potential for combined photothermal and photodynamic therapy. Our bimodal photo-triggered combination therapy amplifies immunogenic cell death by releasing damage-associated molecular patterns (DAMPs) such as HMGB1 and CRT, while simultaneously preventing the immune-evading protein CD47. This study presents a potential strategy to overcome challenges faced by conventional phototherapies, such as the overexpression of heat shock proteins (HSPs) and the hypoxic tumor microenvironment. By validating the synthesis of these new PdAsNPs and their synergistic therapeutic effects, we introduce a promising new anticancer treatment approach for non-small cell lung cancer.

2. Materials and methods

2.1. Materials

Sodium arsenite ($NaAsO_2$) was purchased from Fisher Scientific (Loughborough, UK). Sodium tetrachloropalladate(II), poly(polyvinylpyrrolidone) (Mw = 29 kDa), and sodium borohydride were purchased from Sigma-Aldrich (Louis, MO, USA). A549 and MRC-5 cells were purchased from ATCC. CRT-Alexa Fluor 488 (#ab196158) and HMGB1 PE (#ab225042) were acquired from Abcam (USA), and CD47 (#556046) from BD Biosciences (California, USA).

2.2. Synthesis of AsNPs

A 2 mL aliquot of a 10 mM As(III) aqueous solution was mixed with 24 mL of DI water in a transparent borosilicate glass vial. Freshly prepared 100 mM $NaBH_4$ aqueous solution (1.2 mL) was rapidly injected into the previously prepared As precursor solution and incubated at 25 °C for 18 h without any disturbance. A light-yellow color developed after 10 min of incubation and turned deep yellowish-brown within 6 h. The solution was incubated for 18 h to ensure the complete decomposition of the remaining $NaBH_4$ with full aging. The product was centrifuged for 15 min at 10 000 rpm, washed with DI water, and the obtained AsNPs were redispersed in 4 mL DI water.

2.3. Synthesis of PdAsNPs *via* galvanic replacement

The as-synthesized AsNPs (4 mL), 2 mL of PVP (MW 29 kDa, 150 mg/10 mL) aqueous solution, and 1 mL of 10 mM Na_2PdCl_4 aqueous solution were sequentially added to a 10 mL transparent borosilicate glass vial. The mixture was allowed to stand in a water bath at 80 °C for 6 h, without any mechanical disturbance. The black product was centrifuged for 15 min at 10 000 rpm, washed with DI water for purification, and re-dispersed in 8 mL of DI water for further characterization.

2.4. Characterization

The morphology and size of the NPs were characterized using an energy-filtering TEM (LIBRA 120, Carl Zeiss, Germany). Cs-corrected scanning TEM (JEOL, Japan) was used to obtain the HR-TEM images and EDS mapping. High-resolution field-emission SEM (SU8010, Hitachi High Technology Corporation, Japan) was used to obtain the SEM images. X-ray analyses included XPS (K-Alpha+, Thermo Fischer Scientific, USA) and X-ray diffraction (XRD, SmartLab, Rigaku, Japan). UV-Vis-NIR spectra were recorded on a UV-Vis spectrophotometer (Lambda-465, PerkinElmer, USA). The elemental composition was quantified using ICP-MS (Agilent7900, Agilent Technologies, USA). OCLA Surgical Laser Accessories (LVI Technology Co., Republic of Korea) were used to irradiate the target using NIR radiation.

2.5. Cell culture and laser irradiation

The A549 human lung cancer cell line and normal lung cell line MRC-5 was used to investigate the effect of PdAsNPs on cell growth. Dulbecco's modified Eagle's medium (DMEM) supplemented with 10% FBS (Gibco), 1% penicillin, streptomycin (P/S, Corning, 100×), and phenol red was used for the cell cultures. Cell cultures were performed at 37 °C and 5% CO_2. For cell dissociation, 0.25% Trypsin–EDTA (1×, Gibco) was used after washing with Dulbecco's phosphate-buffered saline (DPBS, 1×, Gibco). Prior to irradiation experiments, desired cells were cultured in 96-well plates until they reached approximately 80% confluency. Following treatment with PdAsNPs, the cells were incubated for 6 h prior to laser exposure. Laser irradiation was performed using an 808-nm diode laser at a power output of 2 W, applied for 1 to 5 min per well. The laser beam was directed uniformly across each well, facilitated by gentle swirling of the plate to ensure even exposure. The distance between the laser source and the surface of the culture media was maintained at 4 cm. All irradiation procedures were conducted at ambient temperature within a laminar airflow hood to maintain sterility and prevent contamination.

2.6. Cell viability

The cells were seeded in 96-well cell culture plates at a density of 5×10^4 cells per mL and incubated for 24 h. Control groups

included untreated cells, cells treated with PdAsNPs without laser irradiation, and cells exposed to laser alone. The next day, the cells were treated with PdAsNPs, incubated for 6 h, and irradiated with an 808-nm laser for 1–5 min as mentioned in Section 2.7. A resazurin based cell viability assay was performed after 24 h of incubation. The wells were washed with PBS, 10% alamarBlue (#DAL1025AB, Thermo Fisher Scientific) was added to each well, and the wells were incubated at 37 °C in a CO_2 incubator for 30 min. Color changes were measured using a multi-reading spectrometer (BioTek, Winooski, Vermont, USA). The excitation and emission wavelengths for the fluorescence measurements were 530 and 560 nm, respectively and fluorescence intensity was normalized to untreated controls and expressed as percentage cell viability.

2.7. Clonogenic assay

A549 cells were incubated for 24 h after the PdAsNP (1 μg mL^{-1}) treatment and laser irradiation. Cells were harvested using 0.25% trypsin–EDTA, centrifuged, and reseeded at an estimated density of 150 cells per 60-mm dish and incubation for 10 days. A fixative containing 70% ethanol and staining solution containing 0.5% crystal violet dye was used to fix the cells. The dishes were gently washed thrice with DI water after overnight staining. To calculate the plating efficiency (PE) and survival fraction (SF), colonies were counted and the following formulas were applied:

$$\mathrm{PE} = \frac{\text{Number of colonies formed}}{\text{Number of cells seeded}} \times 100 \quad (1)$$

$$\mathrm{SF} = \frac{\text{Number of colonies formed after treatment}}{\text{Number of cells seeded} \times \mathrm{PE} \times 100} \quad (2)$$

2.8. Cellular uptake assay

Cellular uptake of FITC-conjugated PdAsNPs was investigated using flow cytometry, and fluorescence images were obtained using confocal microscopy. A549 cells were exposed to 1 μg mL^{-1} PdAsNPs and incubated for 6 h in 37 °C in a 5% CO_2 incubator. Afterwards, cells were washed twice with PBS, trypsinized, centrifuged at 1000 rpm for 3 min, and resuspended in PBS. As previously described, side scattering was used to measure intracellular NPs uptake. As per the manufacturer's guidelines, A549 cells were stained with CellMask deep red actin tracking stain (#A57248) and observed under a microscope to measure cellular uptake of FITC-conjugated PdAsNPs (Olympus, Shinjuku City, Tokyo, Japan).

2.9. Intracellular ROS estimation

Intracellular reactive oxygen species (ROS) generation was assessed utilizing 2′,7′-dichlorodihydrofluorescein diacetate (DCF-DA; Thermo Fisher Scientific, Waltham, MA, USA; #D399), a non-fluorescent, cell-permeable probe. A549 cells were seeded in 6-well plates and incubated overnight to facilitate attachment. Subsequently, the cells were treated with PdAsNPs at a concentration specified (1 μg mL^{-1}) and either subjected to an 800 nm laser (irradiation time: 3 min; power density: 2 W cm^{-2}) or maintained as treated controls. Post-treatment, the cells were washed twice with PBS and incubated with a 10 μM DCF-DA solution prepared in PBS for 30 min at 37 °C in the dark. During this incubation, intracellular esterases cleaved the acetate groups of DCF-DA, converting it into 2′,7′-dichlorodihydrofluorescein (DCF-H), which reacts with intracellular ROS to form the fluorescent compound 2′,7′-dichlorofluorescein (DCF). Following incubation, the cells were washed with PBS, and fluorescence images were captured using an Olympus fluorescence microscope (Olympus, Shinjuku City, Tokyo, Japan) at excitation wavelengths of 492–495 nm and emission wavelengths of 517–527 nm.

2.10. Flow cytometry

A549 cells were exposed to PdAsNPs (1 μg mL^{-1}) and an 800 nm laser at 2 W cm^{-2} for 3 min and incubated for 24 h. Cells were washed with cold PBS and incubated for 40 min in the dark with CRT-Alexa Fluor 488 at a final concentration of 1 : 100 and HMGB1 PE at 1 : 1000. Samples were collected immediately after staining and analyzed using a FACSVerse system (BD Biosciences, Seoul, Republic of Korea).

2.11. qRT-PCR

The expression of genes related to antioxidants and those associated with ICD mRNA was evaluated using qRT-PCR. A549 cells were treated with PdAsNPs (1 μg mL^{-1}) and exposed to an 800 nm laser at 2 W cm^{-2} for 3 min, followed by incubation for 24 h. TRIzol reagent (Invitrogen) was used to extract RNA, according to the manufacturer's instructions. The Superscript II reverse transcriptase kit (Invitrogen) was used to synthesize the cDNA. Real-time PCR was conducted using IQ SYBR Green Supermix (BD Biosciences) on a Bio-Rad CFX96TM RealTime System. Primers listed in Table 1 (supplementary information) were purchased from Macrogen (Seoul, Korea). The results were normalized using β-actin as the control gene.

2.12. Statistical analysis

The results are presented as mean ± standard deviation of three independent experiments. The data were evaluated using one-way analysis of variance (ANOVA) using Prism software version 9.0 among multiple groups. A more detailed description has been added to the figure legend. Significance is denoted by $^{*}p < 0.05$, $^{**}p < 0.01$, and $^{***}p < 0.001$.

3. Results and discussion

3.1. Synthesis of PdAsNPs

The galvanic replacement reaction for elemental substitution and nanostructural transformation was performed on monodisperse AsNP templates synthesized *via* chemical reduction of sodium arsenite (As^{3+}). The AsNPs were stable and fully dispersed in the solution, even without the addition of polymers or surfactants. The residual As source and reducing agent were removed and a Pd precursor solution (Pd^{2+}) was added to the

AsNPs in deionized (DI) water. The amount of Pd, reaction temperature, and additives were optimized to achieve elemental substitution while maintaining the overall external morphology and dispersion. The addition of polyvinylpyrrolidone (PVP) and moderate heat (80 °C) below the boiling point of the solvent were essential to obtain the desired PdAsNPs with uniform substitution.

The NP dispersion changed from yellowish-brown to black in the presence of Pd. This was confirmed by the bathochromic shift from 291 to 430 nm in the UV-Vis-NIR region (Fig. 1A). The size, morphology, and distribution of NPs before and after the reaction were analyzed by transmission electron microscopy (TEM). The monodisperse size distribution of AsNPs was maintained in PdAsNPs (Fig. 1B, 1st column). However, an increase in the particle diameter from 46 ± 2.7 nm to 51 ± 2.2 nm and the presence of hollow interior vacancies in PdAsNPs confirm the formation of nanoshells (counting # = 50) (Fig. 1B, 2nd column). These findings were confirmed by scanning electron microscopy (SEM) (Fig. 1B, 3rd column).

When an element in a solid-state nanostructure comes into contact with another ionic species, the difference in its reduction potential causes a spontaneous redox reaction, resulting in galvanic replacement. The AsNPs formed *via* rapid reduction consisted of metallic phase As^0, except for a small amount of surface oxidation through atmospheric contact. This was evidenced by the TEM image of the noise-level O-Kα line of the grid-surface formvar polymer film and the high-angle annular dark-field scanning transmission electron microscopy/energy dispersive X-ray spectroscopy (HAADF-STEM/EDS) image of the As-Kα line (Fig. 1C, top).

A high reduction potential was achieved by the addition of Pd ($Pd^{2+}|Pd^0$ = 0.987 V *vs.* standard hydrogen electrode (SHE)), which is primarily associated with the oxidation of As^0 ($As^{3+}|As^0$ = 0.240 V *vs.* SHE) and further oxidation of the as-formed As^{3+} owing to galvanic replacement ($As^{5+}|As^{3+}$ 0.560 V *vs.* SHE).[16,26] The HAADF-STEM/EDS mapping of PdAsNPs exhibited a hollow nanoshell structure, with each shell structure comprising concentrated Pd and colocalization of As and O signals (Fig. 1C, bottom), which is consistent with previously observed line profiles (Fig. S1).

3.2. X-ray characterization of PdAsNPs

The composition and crystallinity of AsNPs and PdAsNPs were determined *via* X-ray analysis. The wide-scan X-ray photoelectron spectrum (XPS) of the AsNPs revealed 3s, 3p, and 3d peaks. However, these peaks decreased significantly with the appearance of new Pd peaks in the spectrum of the PdAsNPs (Fig. S2). The deconvoluted As 3d XPS spectrum showed As^0 peaks at 41.4 and 42.1 eV, corresponding to $3d_{5/2}$ and $3d_{3/2}$, respectively, with overlapping spin–orbit components (0.7 eV) with an intensity ratio 0.7. In addition, an As^{3+} peak was observed at 44.8 eV, indicating the oxidation of the surface layer. In contrast, the As

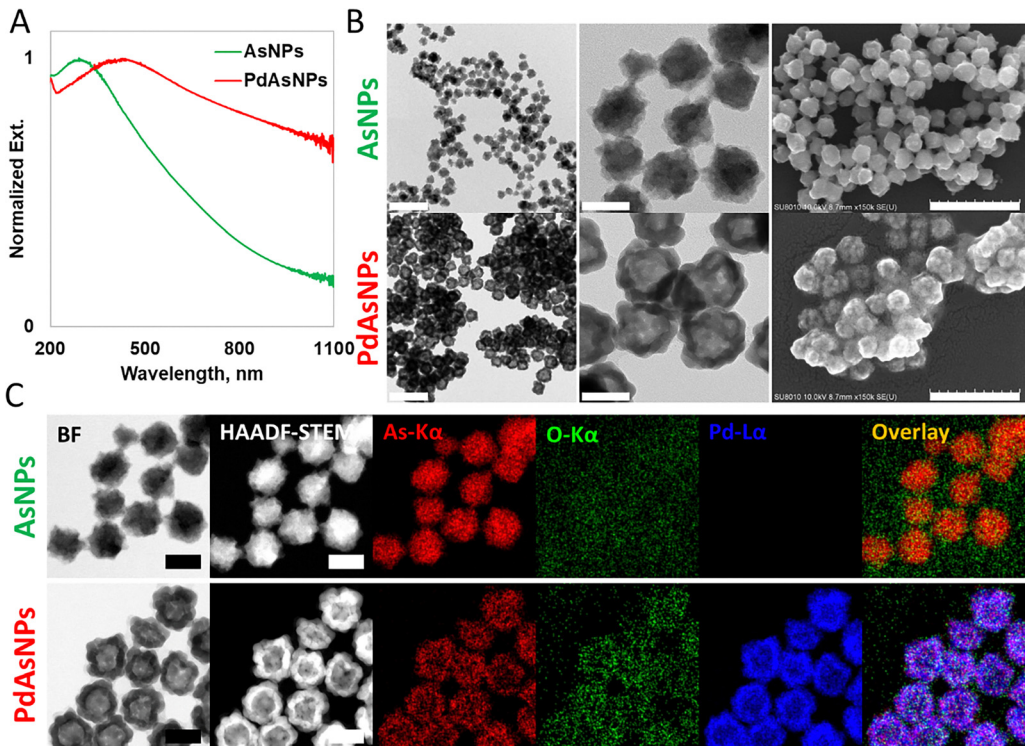

Fig. 1 Characterization of AsNPs and PdAsNPs. (A) UV-Vis-near infrared (NIR) spectra and (B) transmission electron microscopy (TEM) and scanning electron microscopy (SEM) images showing the formation of hollow PdAsNPs. Scale bars: 200 nm (low-magnification, left), 50 nm (higher-magnification, middle), and 300 nm (SEM, right). (C) High-angle annular dark-field scanning transmission electron microscopy/energy dispersive X-ray spectroscopy (HAADF-STEM/EDS) mapping images exhibiting elemental co-distribution. The scale bar is 50 nm.

3d XPS spectrum of PdAsNPs revealed an As^{5+} peak at 46.0 eV, along with small signals for As^{0} and As^{3+}, confirming the oxidation of As during galvanic replacement (Fig. 2A). The Pd 3d XPS spectrum of the PdAs NPs showed Pd^{0} peaks at 335.2 and 340.5 eV, corresponding to $3d_{5/2}$ and $3d_{3/2}$, respectively, with well-separated spin–orbit components (5.3 eV); Pd^{2+} peaks at 336.4 and 341.7 eV), and Pd^{4+} peaks at 338.1 and 343.0 eV (Fig. 2B).

The X-ray diffraction (XRD) pattern of the AsNPs confirmed the presence of As and As_2O_3, whereas that of the PdAs NPs revealed multiple As_2O_5 patterns along with metallic Pd signals. No clear patterns were observed, suggesting that both particles were polycrystalline or partially amorphous, rather than single crystals (Fig. 2C). The intense Si peaks are attributed to the formation of a nanoparticle film on the Si wafer surface. Fast Fourier transform (FFT) and high-resolution (HR) TEM images were used to validate crystallinity information. AsNPs exhibited an amorphous morphology, whereas PdAsNPs exhibited polycrystalline Pd (Fig. 2D).

3.3. PT and PD characterization in a quartz cuvette system

As PdAsNPs showed enhanced absorbance across the entire UV-Vis-NIR wavelength region, photothermal (PT) conversion and photocatalytic (PC) activity were quantitatively characterized under *in vitro* conditions to verify their potential photoresponsive applications. A wavelength of 808 nm, commonly used as a surgical laser because of its fine tissue penetration and negligible hazards, was adopted as the phototriggering source. For the PT conversion test, the temperature elevation of the solution was measured in a quartz cuvette with a diameter of 1 cm on all sides. PdAsNPs exhibited concentration-dependent PT behavior. Inductively coupled plasma mass spectrometry (ICP-MS) was used to determine the elemental composition of PdAsNPs at a maximum temperature of 42.8 °C with an irradiation of 2 W cm^{-2} laser (1200 J) for 600 s at 40 mg Pd/L (ΔT_{40} = 15.1 °C). As the concentration of PdAsNPs decreased, the maximum temperatures decreased to 39.3 °C (ΔT_{20} = 12.2 °C) and 33.6 °C (ΔT_{10} = 5.9 °C) for 20 and 10 mg Pd/L, respectively, under the same conditions. However, a negligible temperature increases of 0.3 °C was observed for 1xPBS without PdAsNPs (Fig. 3A).

The PT conversion efficiency upon laser irradiation was 47.78%, considering the absorption of PdAsNPs and quartz cuvette wall, equilibrium temperature, and surface area (Fig. 3B). Furthermore, repeated temperature changes were observed in the heating–cooling cycle when the laser was turned on and off (Fig. 3C). A comparison of the absorption spectra of PdAsNPs before and after 808-nm laser irradiation (1200 J) confirmed that PT conversion did not affect colloidal stability (Fig. 3D).

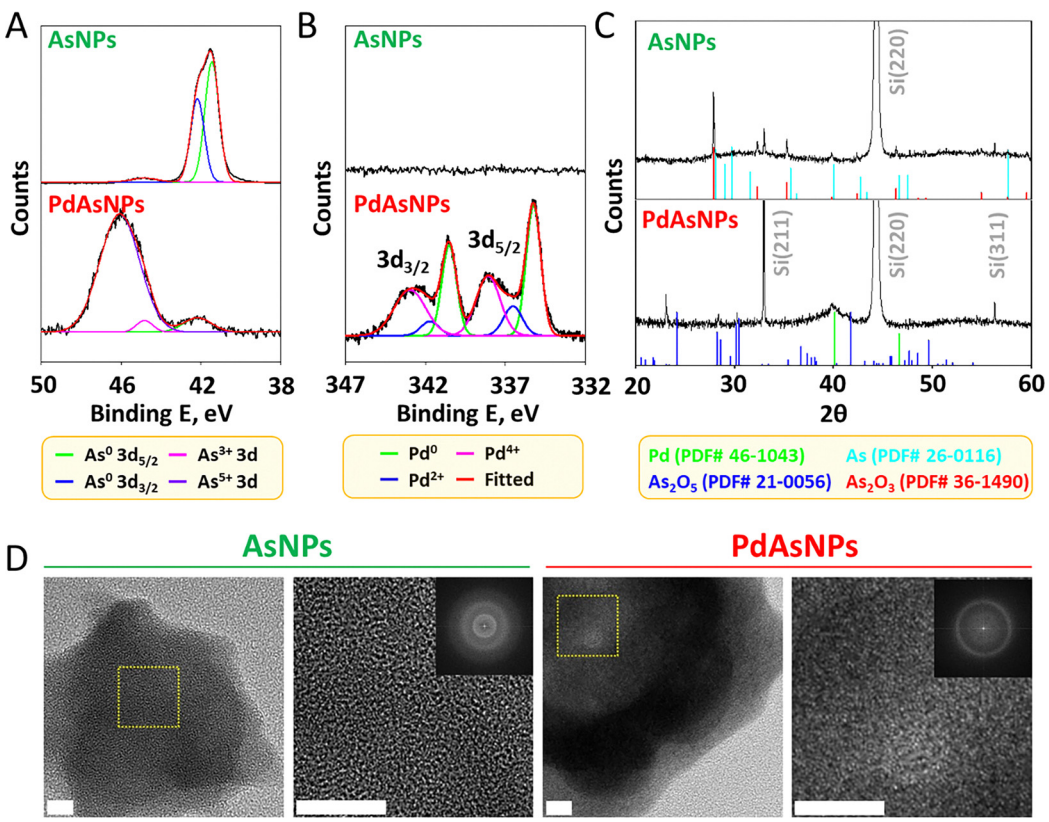

Fig. 2 Composition and crystallinity of AsNPs and PdAsNPs. Deconvoluted X-ray photoelectron (XPS) spectra of (A) As 3d and (B) Pd 3d. (C) X-ray diffraction (XRD) patterns of the AsNPs and PdAsNPs. (D) High-resolution (HR)-TEM and fast Fourier transform (FFT) images of the AsNPs and PdAsNPs. Scale bar, 5 nm.

Cellular temperatures above 42 °C are sufficient to induce cell death during hyperthermic cancer treatment.[27,28] The NPs introduced into the cells are trapped in the endosomes and aggregated in the perinuclear region, which enables higher localized heating than in the case of dispersion in a cuvette. Hence, the observed PT conversion was sufficient for a successful hyperthermic treatment in the designated regions.

The PC activity of semiconducting NPs causes the generation of excited states and the consequent electron transfer to the surrounding medium or molecules, thereby forming highly reactive radical species. Arsenic is likely responsible for the PC activity. Therefore, we evaluated two possible PC pathways associated with the combination of PdAsNPs and PDT. In the the PDT type-I process, the excited electron reacts instantaneously with a dissolved oxygen molecule ($^3O_2$) to form a superoxide radical anion ($O_2^{\bullet-}$), which in turn generates hydroxyl radicals ($^\bullet$OH) to initiate the cytotoxic process.[29,30] To identify the existence of the type-I process, the PdAsNP dispersion was irradiated with an 808-nm laser with methylene blue (MB) as the colorimetric indicator of the photodegradation of the radical species. The MB absorbance at 652 nm with 1× PBS as the negative control of PdAsNPs induced only 3% photodegradation, confirming that there was no contribution from the PD type-I pathway (Fig. 3E). The type-II process involves cell death *via* a lower-energy singlet oxygen-excited state ($^1\Delta_g$). To confirm the generation of singlet oxygen species, we measured the increase in the fluorescence signal of the fluorogenic indicator singlet oxygen sensor green (SOSG) by irradiating it with an 808 nm laser. Tracking the fluorescence signal over time confirmed that the PdAsNPs exhibited a type-II pathway. PdAsNPs produced approximately 5.8 times higher number of ROS than 1× PBS, which is 2.4–3.2 times higher than those of previously reported metal nanomaterials (Fig. 3F).[31] The obtained PD efficiency suggests that 808-nm laser irradiation is sufficient to induce cancer cell ablation in addition to PT conversion-mediated hyperthermia.

3.4. Targeted phototoxicity induced by PdAsNPs

Lung cancer is the leading cause of cancer-related death. Notably, mesenchymal cells of the non-small cell lung cancer (NSCLC) cell line A549 are resistant to chemotherapy. The effectiveness and selectivity of phototherapy for the treatment of primary cancers has recently been recognized as promising. Using phototherapeutic agents, light energy can be converted into heat (PTT) and ROS (PDT).[30] Hence, we analyzed the cytotoxic effects of PdAsNPs in combination with 808-nm laser irradiation using the Alamar blue assay. In addition, near-infrared lasers can be used for optical treatment because visible light penetrates only a limited amount of soft tissue.[30] To initially assess the impact of PdAsNPs, concentrations ranging from 0.5 to 10 μg mL^{-1} were applied to normal lung cells (MRC-5). It was observed that a 5 μg mL^{-1} concentration of PdAsNPs resulted in approximately 20% cell death after 24 h of exposure (Fig. S3). Consequently, a concentration of 1 μg mL^{-1} PdAsNPs was applied to A549 cancer cells, both with and without laser irradiation. Laser irradiation was administered for durations of 1 to 5 min, followed by incubation periods of 24, 48, and 72 h, as outlined in the methodology. Notably, the group subjected to

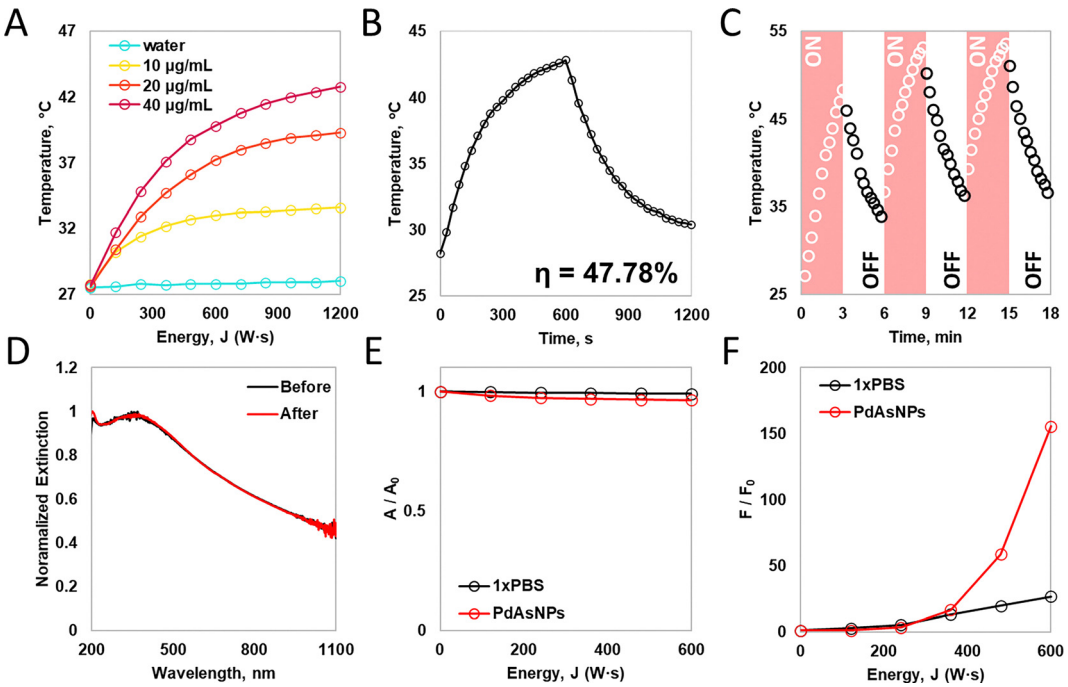

Fig. 3 Photothermal conversion and photocatalytic activity of PdAsNPs under NIR irradiation. (A) Temperature elevation of PdAsNP dispersion under 808-nm laser irradiation at varying concentrations. (B) Heating–cooling curve for PT efficiency and (C) repeated heating–cooling cycling during laser on and off. 2 W of 808-nm laser irradiation was performed against 50 μg mL^{-1} concentration. (D) Colloidal thermal stability under laser irradiation. Photocatalytic (E) type-I and (F) type-II activities in quartz cuvette system.

3 min of laser treatment exhibited a significant reduction in A549 cell viability (Fig. 4A and B). Therefore, this treatment condition was selected for subsequent assays.

We further confirmed this inhibition of cancer cells using a clonogenic assay. PdAsNPs reduced the formation of cancer cell colonies, and this effect was further augmented by laser irradiation (Fig. 4C). The *in vitro* results confirmed the synergistic cytotoxic effect of photothermal ablation and ROS generation induced by the laser-irradiated PdAsNPs. Phototherapeutic agents convert light energy into heat and ROS *via* phototransduction.[29] Advances in endoscopic and fiberoptic light delivery techniques have enabled minimally invasive treatment of many solid tumors, including those in sensitive anatomic areas that may not be accessible through surgery.[32,33] The use of photosensitive materials in conjunction with laser irradiation produces localized hyperpyrexia (PTT) or cytotoxic. ROS, resulting in the death of tumor cells surrounding the irradiation site.[32] An important aspect of ICD is that it triggers a T cell-adaptive immune response and induces long-term immunological memory, making it a promising approach for eliminating cancerous cells.[34]

3.5. Cellular uptake of PdAsNPs

To investigate cellular uptake and endocytosis, PdAsNPs were conjugated with fluorescein isothiocyanate (FITC)–poly(ethyl glycol) (PEG)–SH. After PdAsNP treatment and laser exposure, the cells were harvested, washed three times with PBS, and analyzed using flow cytometry or confocal microscopy. We used two flow cytometry methods to detect internalization of PdAsNPs in cancer cells. The side scattering channel (SSC) represents the scattered light emitted from the incident laser (488 nm) at an angle of 90°. The SSC is typically used to identify the complexity or granularity of the internal structure of a cell. Enhanced SSC intensity is associated with enhanced cell complexity after nanoparticle internalization.[35,36] The fluorescence intensity of FITC was determined by flow cytometry. Cellular granularity significantly increased in the group treated with PdAsNPs and the group treated with PdAsNPs and laser irradiation (Fig. 5A).

The fluorescence intensity showed that FITC-labeled PdAsNPs were taken up by cancer cells (Fig. 5B). Moreover, the intensity of FITC increased in the combination group (Fig. 5C), which supports our hypothesis that the chemosensitization effect is enhanced by the thermal energy provided by PTT, which increases membrane permeabilization and enables cellular uptake of NPs.

3.6. ROS production and modulation of oxidative stress-associated genes

To demonstrate intracellular ROS generation by PdAsNPs and laser-irradiated PdAsNPs, a H_2DCFDA probe was used to observe the green fluorescence intensity in cancer cells, which indicated the presence of intracellular ROS. The intensity exhibited by the laser-irradiated PdAsNPs in cells was nearly two times higher than that exhibited by cells treated with PdAsNPs alone (Fig. 6A and B). This indicated that a higher amount of ROS was produced in the laser-irradiated group. Intracellular ROS such as $^1O_2$, $O_2^{-\bullet}$, H_2O_2, $^\bullet OH$, and $ROO^\bullet$ *via* distinct mechanisms, such as endoplasmic reticulum-induced ROS during the metabolism of As, mitochondrial electron transport chain complexes, and the action of a membrane-associated enzyme such as nicotinamide adenine dinucleotide phosphate (NA(P)H) oxidase (Nox).[37] Furthermore, arsenic disrupts mitochondrial membrane potential, facilitates ROS accumulation, and activates apoptotic factors.[38] ROS accumulation interferes with cellular antioxidant enzyme systems such as glutathione (GSH) peroxidase (GPx), superoxide dismutase (SOD), and catalase (CAT).[37] PDT enables the production of toxic singlet oxygen ($^1O_2$) *via* energy transfer (type II) between the triplet state and O_2. Cancer cells equilibrate to oxidative stress *via* glutathione (GSH); hence, many GSH-targeted biomaterials have been developed to disrupt redox homeostasis.[38] Furthermore, the modulation of antioxidant enzyme-related mRNA expression indicates that cells attempt to maintain homeostasis by activating their defence against oxidative stress.[39] Antioxidant-related gene expression was evaluated in cells treated with laser-irradiated PdAsNPs. GPx mRNA expression did not change in the group with non-irradiated PdAsNPs (Fig. 6C) but was significantly reduced in the laser-irradiated group. Abundant GPx eliminates intracellular reactive oxygen species (ROS) in cancer cells and inhibits apoptosis, resulting in resistance. GPx inhibitors can synergize PDT efficacy *via* ROS-mediated apoptotic cell death in cancer.[37,38] Moreover, there was no significant difference in the mRNA expression of SOD and CAT in the non-irradiated PdAsNP group; however, the expression of these two genes was significantly increased in the irradiated PdAsNP group, which could increase or decrease the amount of ROS, causing oxidative stress and aberrant cell signalling or disrupting cell signalling and homeostasis, respectively. CuZn-SOD and SOD1 are homodimeric enzymes found in cytoplasmic, nuclear, and lysosomal compartments. Many chemobiological factors influence SOD mRNA expression, including heat shock and oxidative stress.[40,41] The conversion of H_2O_2 to O_2 leads to tumor hyperoxia and may ultimately enhance PDT efficacy. These results indicate that PdAsNP cytotoxicity may be mediated by disruption of cellular homeostasis and overproduction of intracellular ROS.

3.7. Synergistic effect of phototherapy on ICD

Organic NPs can be used either as a localized source for ICD-inducing treatments or to enhance external energy fields to minimize tissue destruction. Several photosensitizers induce ICD through the externalization of calreticulin (CRT), ATP, heat shock proteins (HSP70 and HSP90), and high-mobility group box proteins (HMGB1).[42] In this study, we investigated whether laser-irradiated PdAsNPs could modulate the immunogenicity of cancer cells. The two most important hallmarks of ICD, CRT and HMGB1, were also investigated. The protein expression of CRT and HMGB1 in both non-irradiated and irradiated PdAsNPs-containing cells was significantly increased (Fig. 6D and E).[43] In addition, the mRNA expression of these DAMP-related molecules was assessed. CRT mRNA expression was enhanced in both treatment groups, whereas HMGB1 mRNA expression was only enhanced in the combination group (Fig. 6F). Comprehensive

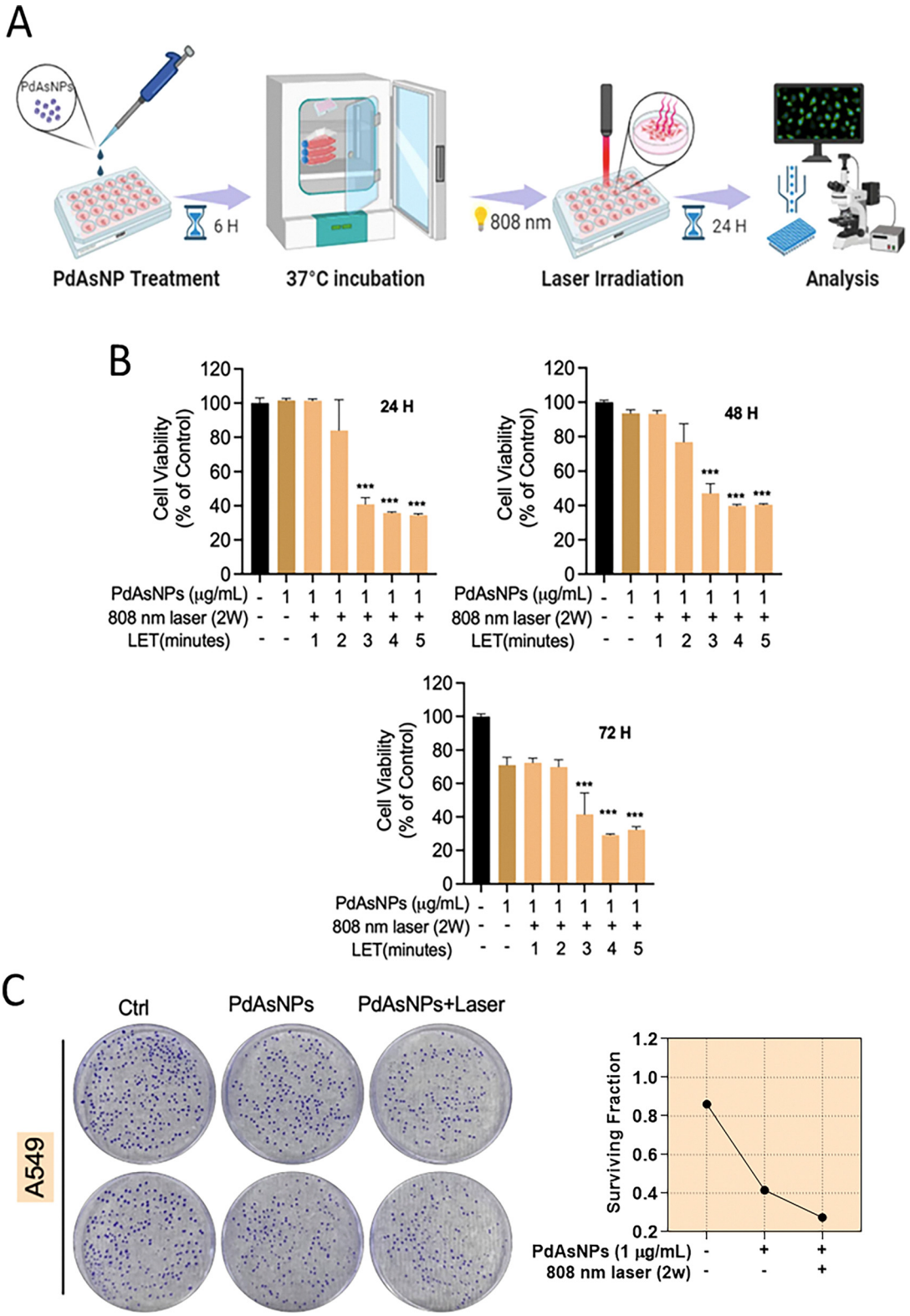

Fig. 4 The combination of PdAsNPs and laser irradiation (808-nm) inhibited the growth of lung cancer cells. (A) Illustration of PdAsNP exposure and laser irradiation, (B) effect on cell viability after 24, 48, and 72 h of PdAsNPs and 808-nm laser-irradiated PdAsNPs, and (C) effect of PdAsNPs and 808-nm laser-irradiated PdAsNPs on colony-forming units. Dunnett's multiple comparison test coupled with a one-way ANOVA was used to determine the statistical significance and was denoted as ***$p < 0.001$.

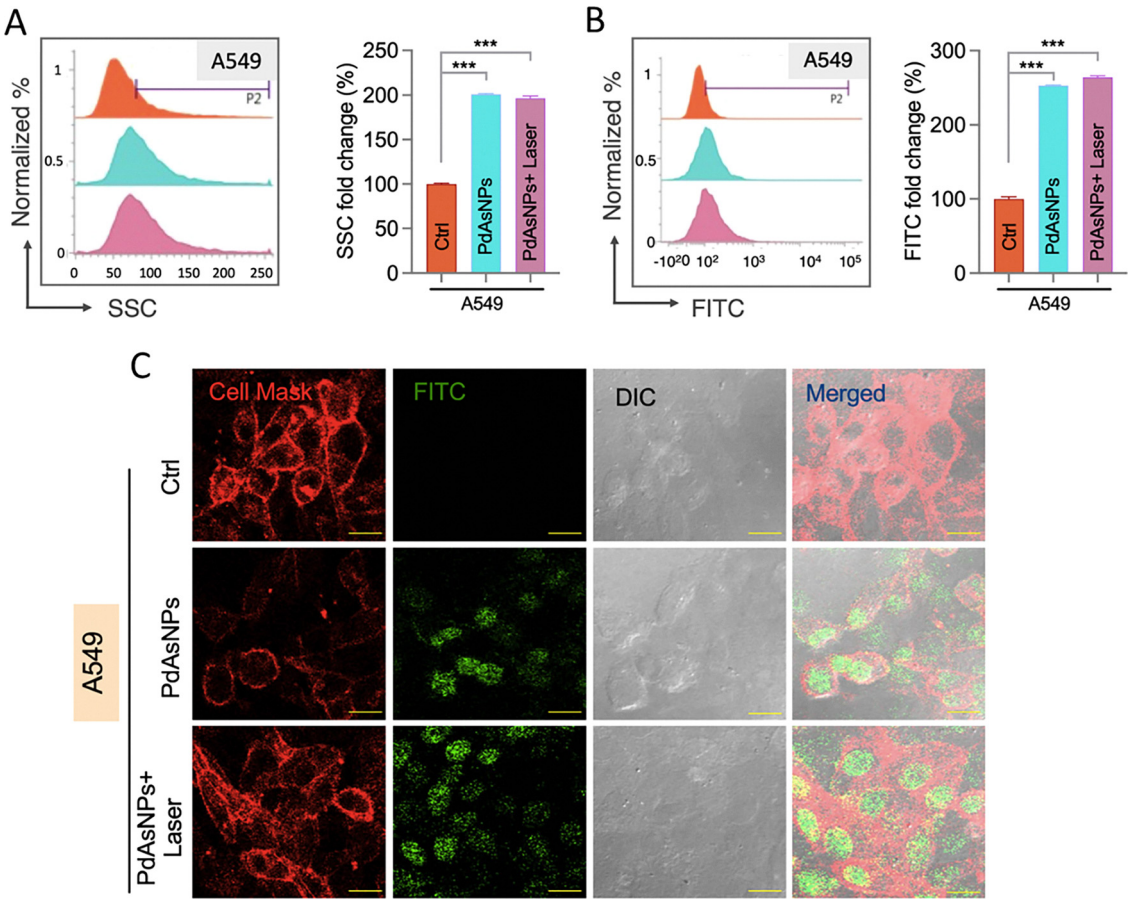

Fig. 5 Uptake of nanoparticles by lung cancer cells. (A) Flow cytometry and side scattering channel (SSC) signifying the increased granularity of A549 cells after PdAsNP intake. (B) Flow cytometry of cells treated with FITC-PdAsNPs and irradiated FITC-PdAsNPs, where the intensity of fluorescence increased after 24 h. (C) Immunofluorescence staining for the visualization of FITC-PdAsNPs in A549 cells. Scale bar: 100 μm. Dunnett's multiple comparison test coupled with a one-way ANOVA was used to determine statistical significance and was denoted as ***$p < 0.001$.

in vitro studies revealed that some PDT and PTT effectively suppressed the CD47 protein (the "don't eat me" signal) and released several DAMPs (*e.g.*, ATP, HMGB1, CRT, ERp57, and HSP9).[42,43] Hence, the effects of both non-irradiated and irradiated PdAsNPs on CD47 expression in cancer cells should be investigated. CD47 expression decreased after the combination therapy (Fig. 6G). CRT is expressed both in the cytosol and on the cell surface, and the ER retrieval sequence KDEL (Lys-Asp-Glu-Leu) requires CRT translocation from the lumen to the cytosol, and ultimately to the cell surface.[44] Immunogenic stimulation induces translocation of CRT to the cell surface, which encounters dendritic cells (DCs), resulting in an "eat me" signal and triggering the engulfment of apoptotic cells.[45]

Furthermore, HMGB1 translocation from the nucleus to the cytosol and the extracellular space acts as an "alarm" and interacts with various receptors on DC surfaces, including Toll-like receptor 4 (TLR4).[46] This may account for the synergistic toxicity observed in the combination group compared with that in the untreated group. Many reports have shown that CRT exposure on dying cell surfaces during ICD is influenced by an apical module that produces oxidative reactions. However, pretreatment with L-histidine or overexpression of GPx4, an antioxidant enzyme, reduces PDT-induced ecto-CRT.[46]

In this context, cells irradiated with PdAsNPs showed inhibited GPx mRNA expression. However, the expression of other antioxidant-related genes was enhanced after combination therapy, likely because of redox regulation against oxidative stress overload. Overall, the expression of the most important DAMP molecules, HMGB1 and CRT, was promoted by the NPs in the combination group. However, the gene expression of HMGB1 was increased only in the combination group. In addition to regulating neutrophil migration, CD47 is involved in the co-stimulation of T cells. Notably, blocking the interaction of CD47 with its natural ligand SIRPα in mouse xenograft models stimulates phagocytosis and prevents solid human malignancies.[45,47,48] In this study, CD47 expression was inhibited after phototherapy, which ultimately enhanced immune stimulation. This suggests that PdAsNPs mediate PDT in lung cancer cells and may play an important role in the regulation of antitumor immunity. Moreover, HSP70 and HSP90 may serve as tumor suppressors or inducers in the tumor microenvironment, are critical for energy metabolism under stress conditions, and promote therapeutic resistance.[49]

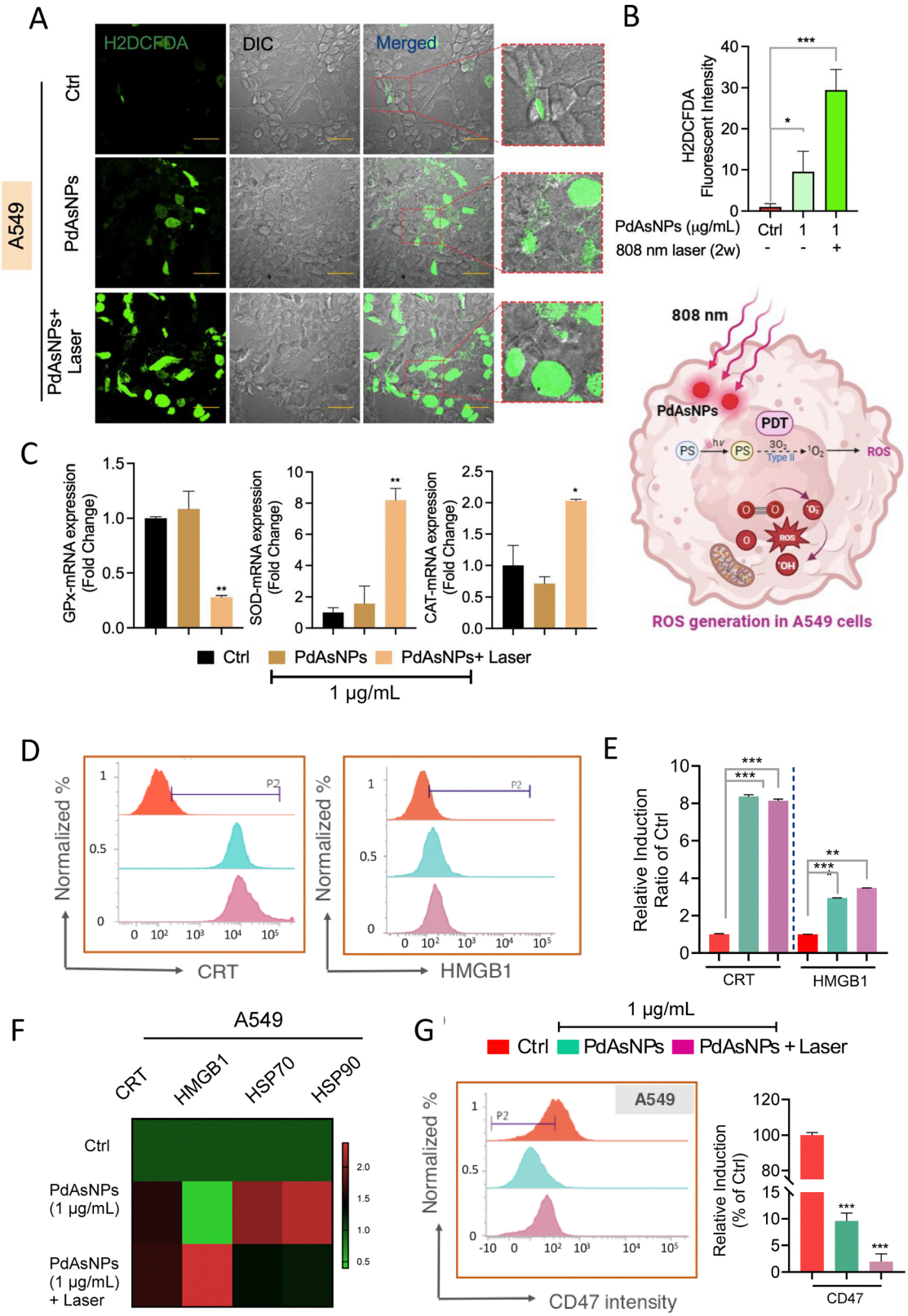

Fig. 6 PdAsNP-induced anticancer immune response through damage-associated molecular patterns (DAMPs). (A) Intracellular reactive oxygen species (ROS) detected using H2DCFDA dye in live cells and assessed by immunofluorescence microscopy. Scale bar: 100 μm. (B) The fluorescence intensity of H2DCFDA. (C) Effect on the mRNA expression of glutathione peroxidase (GPX), superoxide dismutase (SOD), and catalase (CAT). (D) Flow cytometry histograms showing CRT and HMGB1 protein intensity using fluorescently tagged antibodies (CRT–Alexa Fluor 488, HMGB1–PE). Red, green, and purple lines represent untreated control, PdAsNP-treated, and PsAsNPs + laser-treated groups, respectively. (E) Quantification of CRT and HMGB1 fluorescence intensity between the indicated groups (F) Heatmap showing relative mRNA expression levels of CRT, HMGB1, HSP70, and HSP90, where green indicates

lower expression and red indicates higher expression. (G) Flow cytometry histogram of CD47 protein intensity detected using CD47–PE antibody. The accompanying bar graph shows relative intensity differences between untreated control, PdAsNP-treated, and PsAsNPs + laser-treated groups. Red, green, and purple indicate the same groups as in (D). Dunnett's multiple comparison test coupled with a one-way ANOVA was used to determine statistical significance and was denoted as $*p < 0.05$; $**p < 0.01$; and $***p < 0.001$.

The therapeutic efficacy of cancer treatment has been limited by two major obstacles: (1) the hypoxic tumor microenvironment, in which ROS, especially $^1O_2$, are restricted,[50,51] and (2) the overexpression of HSPs with increasing temperature, which reduces therapeutic efficacy and increases the chance of recurrence.[51] Therefore, effective combination strategies to overcome hypoxia and moderate HSP expression are essential for improving cancer phototherapy. This study demonstrates that a combination of PdAsNPs and phototherapy could not only moderate the cancer-protective switches HSP70, HSP90, and CD47, but also enhance ICD in lung cancer.

4. Conclusions

In this study, we synthesized AsPd nanoparticles (PdAsNPs) *via* galvanic replacement and evaluated the anticancer activity of PdAsNPs irradiated with an 808-nm laser. A spontaneous galvanic reaction between the AsNPs and Pd(II) ions generated nanoshell structures. Although the initial metallic As composition underwent structural alterations, the As oxide, which exhibits intrinsic anti-cancer properties, was retained in the PdAsNPs. The introduction of plasmonic Pd and nanoshell characteristics increased the photothermal conversion efficiency to 47.78% and resulted in a 5.8-fold singlet oxygen production upon irradiation with an 808-nm near-infrared (NIR) laser. PdAsNPs exhibited cytotoxicity in lung cancer cells, which was improved by NIR laser irradiation, resulting in the generation of intracellular reactive oxygen species in the A549 human lung cancer cell line and modulation of oxidative stress-related genes. The combination of PdAsNPs and NIR laser irradiation stimulates immunogenic cell death by releasing damage-associated molecular patterns, such as HMGB1 and CRT, while preventing the immune escape protein CD47. This combined action decreases the expression of heat shock proteins, which likely enhances the effects of photothermal therapy. Our results highlight the ability of PdAsNP-mediated photothermal therapy and photodynamic therapy to induce immune modulation in tumors and synergistically combat lung carcinoma cells.

Author contributions

S. W. Kim: methodology, formal analysis, visualization, investigation, writing – original draft; M. Negi: investigation, formal analysis, methodology, writing – original draft, review and editing; Y. Heo: formal analysis, investigation; N. Kaushik: review and editing, formal analysis, funding acquisition, visualization; A. Jaiswal: formal analysis, investigation; E. H. Choi: supervision, project administration, formal analysis, funding acquisition; N. K. Kaushik: conceptualization, supervision, project administration, writing – review and editing, formal analysis, funding acquisition; H. Jang: conceptualization, supervision, project administration, writing – review and editing, formal analysis, funding acquisition.

Conflicts of interest

The authors have declared no conflict of interest.

Data availability

Data supporting the findings of this study are available in the supplementary information (SI) of this article. Supplementary information: The supplementary information includes; primer sequences used in the study, EDS line profile of AsNPs and PdAsNPs, wide scan XPS spectra of AsNPs and PdAsNP, and effect on cell viability on normal lung cells (MRC-5) after 24 and 48 hours of incubation with PdAsNP. See DOI: https://doi.org/10.1039/d5ma00784d.

Acknowledgements

This work was supported by the National Research Foundation of Korea (NRF) funded by the Korean government (Grant No. RS-2025-00515574, NRF-2022R1A2C4001692, RS-2021-NR060112).

References

1 R. N. Ratnaike, *Postgrad Med. J.*, 2003, **79**, 391–396.
2 J. O. Fatoki and J. A. Badmus, *J. Hazard. Mater. Adv.*, 2022, **5**, 100052, DOI: 10.1016/j.hazadv.2022.100052.
3 B. E. Hettick, J. E. Cañas-Carrell, A. D. French and D. M. Klein, *J. Agric. Food Chem.*, 2015, **63**, 7097–7107.
4 Y. Liu, A. Luchini, S. Martí-Sánchez, C. Koch, S. Schuwalow, S. A. Khan, T. Stankevič, S. Francoual, J. R. L. Mardegan, J. A. Krieger, V. N. Strocov, J. Stahn, C. A. F. Vaz, M. Ramakrishnan, U. Staub, K. Lefmann, G. Aeppli, J. Arbiol and P. Krogstrup, *ACS Appl. Mater. Interfaces*, 2020, **12**, 8780–8787.
5 B. Kousar, D. J. Carrad, L. Stampfer, P. Krogstrup, J. Nygård and T. S. Jespersen, *Nano Lett.*, 2022, **22**, 8845–8851.
6 P. C. Chen, G. Shen, H. Chen, Y. G. Ha, C. Wu, S. Sukcharoenchoke, Y. Fu, J. Liu, A. Facchetti, T. J. Marks, M. E. Thompson and C. Zhou, *ACS Nano*, 2009, **3**, 3383–3390.
7 N. Dyakonova, S. A. Karandashev, M. E. Levinshtein, B. A. Matveev, M. A. Remennyi and A. A. Usikova, *Infrared Phys. Technol.*, 2021, **117**, 103867, DOI: 10.1016/j.infrared.2021.103867.
8 M. Sönksen, K. Kerl and H. Bunzen, *Med. Res. Rev.*, 2022, **42**, 374–398.

9 J. Hu, Y. Dong, L. Ding, Y. Dong, Z. Wu, W. Wang, M. Shen and Y. Duan, *Signal Transduction Targeted Ther.*, 2019, **4**(1), 28, DOI: 10.1038/s41392-019-0062-9.
10 X. Fu, Q. R. Liang, R. G. Luo, Y. S. Li, X. P. Xiao, L. L. Yu, W. Z. Shan, G. Q. Fan and Q. Tang, *J. Mater. Chem. B*, 2019, **7**, 3088–3099.
11 X. Wang, Y. Hu, J. Mo, J. Zhang, Z. Wang, W. Wei, H. Li, Y. Xu, J. Ma, J. Zhao, Z. Jin and Z. Guo, *Angew. Chem.*, 2020, **132**, 5189–5196.
12 I. Kalyan, T. Pal and A. Pal, *MRS Commun.*, 2019, **9**, 270–279.
13 S. Kang, Y. G. Gil, D. H. Min and H. Jang, *ACS Nano*, 2020, **14**, 4383–4394.
14 G. Yim, S. Kang, Y. J. Kim, Y. K. Kim, D. H. Min and H. Jang, *ACS Nano*, 2019, **13**, 3434–3447.
15 S. Kang, G. Yim, S. Y. Chae, S. Kim, Y. G. Gil, Y. K. Kim, D. H. Min and H. Jang, *ACS Appl. Mater. Interfaces*, 2022, **14**, 40513–40521.
16 A. J. Bard, R. Parsons and J. Jordan, *Stand. Potentials Aqueous Solution*, 2017, 1–834.
17 M. Overchuk, R. A. Weersink, B. C. Wilson and G. Zheng, *ACS Nano*, 2023, **17**, 7979–8003.
18 Y. Nakamura, A. Mochida, P. L. Choyke and H. Kobayashi, *Bioconjug. Chem.*, 2016, **27**, 2225–2238.
19 S. Jha, P. K. Sharma and R. Malviya, *Achiev. Life Sci.*, 2016, **10**, 161–167.
20 Y. Ren, Q. Chen, H. Qi and L. Ruan, *Nanomaterials*, 2017, **7**(12), 416, DOI: 10.3390/nano7120416.
21 W. Li, J. Yang, L. Luo, M. Jiang, B. Qin, H. Yin, C. Zhu, X. Yuan, J. Zhang, Z. Luo, Y. Du, Q. Li, Y. Lou, Y. Qiu and J. You, *Nat. Commun.*, 2019, **10**(1), 3349, DOI: 10.1038/s41467-019-11269-8.
22 S. Jiang, F. Zhu, Y. Lin, L. Ran, F. Lin, H. Tian, T. Hu, P. Wang and C. Lu, *Mater. Des.*, 2023, **225**, 111590, DOI: 10.1016/j.matdes.2023.111590.
23 H. Nakamura and K. Takada, *Cancer Sci.*, 2021, **112**, 3945–3952.
24 E. E. Sweeney, J. Cano-Mejia and R. Fernandes, *Small*, 2018, **14**(20), 1800678, DOI: 10.1002/smll.201800678.
25 J. Gao, W. Qi Wang, Q. Pei, M. S. Lord and H. Jun Yu, *Acta Pharmacol. Sin.*, 2020, **41**, 986–994.
26 H. Liu, Q. Yang, W. Guo, H. Lin, F. Zhang, J. Zhao, T. Ma, L. Zhao, N. Xu, R. Wang, J. Yu and F. Qu, *Chem. Eng. J.*, 2020, **385**, 123979.
27 D. S. Muckle and J. A. Dickson, *Br. J. Cancer*, 1973, **27**, 307–315.
28 F. Shi, D. Luo, X. Zhou, Q. Sun, P. Shen and S. Wang, *Cell Death Discovery*, 2021, **7**, 227.
29 L. Huang, Y. Xuan, Y. Koide, T. Zhiyentayev, M. Tanaka and M. R. Hamblin, *Lasers Surg. Med.*, 2012, **44**, 490–499.
30 X. Li, J. F. Lovell, J. Yoon and X. Chen, *Nat. Rev. Clin. Oncol.*, 2020, **17**, 657–674.
31 D. K. Chatterjee, L. S. Fong and Y. Zhang, *Adv. Drug Delivery Rev.*, 2008, **60**, 1627–1637.
32 F. Ghorbani, N. Attaran-Kakhki and A. Sazgarnia, *Photodiagn. Photodyn. Ther.*, 2017, **17**, 48–55.
33 L. Xu, J. Liu, J. Xi, Q. Li, B. Chang, X. Duan, G. Wang, S. Wang, Z. Wang and L. Wang, *Small*, 2018, **14**, 1800785.
34 T. Mishchenko, I. Balalaeva, A. Gorokhova, M. Vedunova and D. V. Krysko, *Cell Death Discovery*, 2022, **13**(5), 455.
35 Y. Wu, M. R. K. Ali, K. Dansby and M. A. El-Sayed, *Anal. Chem.*, 2019, **91**(22), DOI: 10.1021/acs.analchem.9b02248.
36 N. K. Kaushik, N. Kaushik, R. Wahab, P. Bhartiya, N. N. Linh, F. Khan, A. A. Al-Khedhairy and E. H. Choi, *Cancers*, 2020, **12**(2), 457.
37 Y. Hu, J. Li, B. Lou, R. Wu, G. Wang, C. Lu, H. Wang, J. Pi and Y. Xu, *Biomolecules*, 2020, **10**(2), DOI: 10.3390/biom10020240.
38 L. Liu, J. R. Trimarchi, P. Navarro, M. A. Blasco and D. L. Keefe, *J. Biol. Chem.*, 2003, **278**, 31998–32004.
39 D. Fu, Y. Wang, K. Lin, L. Huang, J. Xu and H. Wu, *RSC Adv.*, 2023, **13**, 22367–22374.
40 P. Bhartiya, N. Kaushik, L. N. Nguyen, S. Bekeschus, K. Masur, K. D. Weltmann, N. K. Kaushik and E. H. Choi, *Int. J. Mol. Sci.*, 2022, **23**(6), 3120.
41 I. N. Zelko, T. J. Mariani and R. J. Folz, *Free Radic. Biol. Med.*, 2002, **33**, 337–349.
42 A. D. Garg and P. Agostinis, *Photochem. Photobiol. Sci.*, 2014, **13**, 474–487.
43 Y. C. Lu, W. C. Weng and H. Lee, *BioMed Res. Int.*, 2015, **2015**(1), 526524.
44 G. Zeng, M. E. Aldridge, X. Tian, D. Seiler, X. Zhang, Y. Jin, J. Rao, W. Li, D. Chen, M. P. Langford, C. Duggan, A. S. Belldegrun and S. M. Dubinett, *J. Immunol.*, 2006, **177**, 3582–3589.
45 S. P. Jong, F. Gamboni-Robertson, Q. He, D. Svetkauskaite, J. Y. Kim, D. Strassheim, J. W. Sohn, S. Yamada, I. Maruyama, A. Banerjee, A. Ishizaka and E. Abraham, *Am. J. Physiol.: Cell Physiol.*, 2006, **290**(3), C917–C924.
46 A. D. Garg, A. M. Dudek, G. B. Ferreira, T. Verfaillie, P. Vandenabeele, D. V. Krysko, C. Mathieu and P. Agostinis, *Autophagy*, 2013, **9**, 1292–1307.
47 B. Kiss, N. S. Van Den Berg, R. Ertsey, K. McKenna, K. E. Mach, C. A. Zhang, J. P. Volkmer, I. L. Weissman, E. L. Rosenthal and J. C. Liao, *Clin. Cancer Res.*, 2019, **25**, 3561–3571.
48 M. Negi, N. Kaushik, L. N. Nguyen, E. H. Choi and N. K. Kaushik, *Free Radic. Biol. Med.*, 2023, **201**, 26–40.
49 S. Yang, H. Xiao and L. Cao, *Biomed. Pharmacother.*, 2021, **142**, 112074, DOI: 10.1016/j.biopha.2021.112074.
50 Y. Du, J. Han, F. Jin and Y. Du, *Pharmaceutics*, 2022, **14**(9), 1763, DOI: 10.3390/pharmaceutics14091763.
51 G. Zhang, W. Cheng, L. Du, C. Xu and J. Li, *J. Nanobiotechnol.*, 2021, **19**(1), 9, DOI: 10.1186/s12951-020-00749-5.